ARTICLE

BIOTECHNOLOGY and BIOENGINEERING

Nanoelectronic Impedance Detection of Target Cells

Rahim Esfandyarpour,[1,2] Mehdi Javanmard,[2] Zahra Koochak,[1] James S. Harris,[1] Ronald W. Davis[2]

[1]Center for Integrated Systems, Department of Electrical Engineering, Stanford University, Stanford, California; telephone: +1-650-387-5976; fax: (650) 812-1975; e-mail: rahimes@stanford.edu

[2]Stanford Genome Technology Center, 855 California Ave., Palo Alto, California 94304

ABSTRACT: Detection of cells is typically performed using optical fluorescence based techniques such as flow cytometry. Here we present the impedance detection of target cells using a nanoelectronic probe we have developed, which we refer to as the nanoneedle biosensor. The nanoneedle consists of a thin film conducting electrode layer at the bottom, an insulative oxide layer above, another conductive electrode layer above, and a protective oxide above. The electrical impedance is measured between the two electrode layers. Cells captured on the surface of the nanoneedle tip results in a decrease in the impedance across the sensing electrodes. The basic mechanisms behind the electrical response of cells in solution under an applied alternating electrical field stems from modulation of the relative permittivity at the interface. In this paper we discuss, the circuit model, the nanofabrication, and the testing and characterization of the sensor. We demonstrate proof of concept for detection of yeast cells with specificity. We envision the sensor presented in this paper to be combined with microfluidic pre-concentration technologies to develop low cost point-of-care diagnostic assays for the clinical setting.

Biotechnol. Bioeng. 2014;111: 1161–1169.

KEYWORDS: biosensing; nanotechnology; nanobiotechnology; cell detection; impedance detection

Introduction

The detection and recognition of cells in a complex sample is very important for applications such as medical diagnostics and food safety. In the case of medical diagnostics detection of pathogenic bacterial cells in blood or sputum has applications for diagnosing infectious diseases. For example, in the case of pseudomonas aeruginosa, diagnosis can be achieved by obtaining bacterial cultures from sputum using bronchoalveolar lavage (Nagrath et al., 2007). Mycobacterium also exists in sputum for tuberculosis at concentrations of ~100 cfu/mL (Moon et al., 2009). Detection of circulating tumor cells in blood also has shown to be clinically relevant for early diagnosis of cancer (Talasaz et al., 2009). Evidence shows the presence of circulating tumor cells in blood at concentrations below 100 cells per 10 mL of blood. In the case of food safety, various threats such as *E. coli* 0157 and salmonella have recently emerged. To perform rapid recognition, it would be necessary to rapidly and inexpensively detect low concentrations of pathogenic bacteria in complex sample capable of detecting single bacterial cells. In order to be cost effective for the applications discussed, such platforms should be rapid, sensitive, low in cost, and portable.

Up to date, the gold standard for detection of cells in a complex sample is flow cytometry (Khaw et al., 1982). Typically this involves labeling a target cell with fluorescent antibodies and passing them through a fluorescent detector one by one. Flow cytometry is advantageous given that it is rapid and highly accurate. The main drawback to flow cytometry is the high cost limiting its usage to primarily core facilities, and also the need for labeling the cells in advance.

Many emerging techniques have been published in the literature, which have sought to overcome the limitations associated with flow cytometry. Some groups have sought to lower the cost of the optical instrumentation by using common tools such as cell phone cameras and inexpensive miniaturized optics (Mostafalu and Sonkusale, 2013). Ozcan, for example, has demonstrated a handheld cell phone based flow cytometer (Zhu et al., 2011). Demirci and coworkers demonstrated a lenseless method for counting cells captured on a surface (Moon et al., 2009). Toner and coworkers demonstrated microfluidic channels integrated with microposts (Nagrath et al., 2007), herringbone mixers (Stott et al., 2010), nanotube-based microposts (Chen et al., 2011), and fluid permeable surfaces (Mittal et al., 2012) for rolling capture of circulating tumor cells in blood.

Several other groups have sought to lower the instrumentation cost by moving away from optical detection altogether

Correspondence to: R. Esfandyarpour
Contract grant sponsor: The National Institutes of Health Grant
Contract grant number: P01HG000205
Received 4 June 2013; Revision received 2 December 2013; Accepted 5 December 2013
Accepted manuscript online 12 December 2013;
Article first published online 28 December 2013 in Wiley Online Library (http://onlinelibrary.wiley.com/doi/10.1002/bit.25171/abstract).
DOI 10.1002/bit.25171

and performing the detection electronically (Chaurey et al., 2013). Bashir et al. demonstrated counting of CD4 cells using a microfluidic capture chamber integrated with electrodes for measuring the change in conductivity after the capture cells have been lysed (Aaron et al., 2004). Bashir and coworkers also demonstrated various electrical detection methods for pathogen detection for applications to food safety and bio-threat recognition (Talasaz et al., 2009). Javanmard et al. (2007) demonstrated the use of bioactivated microfluidic channels for capturing target cells while measuring changes in impedance across the channel. They also demonstrated the use of parallel microfluidic channels for increase in throughput of cell capture for pathogenic yeast cells (Javanmard et al., 2012). Additionally Javanmard et al. demonstrated contactless impedance cytometry suitable for counting of single cells and single beads (Emaminejad et al., 2012). Sohns et al. demonstrated the use of antibody functionalized micropores for detecting cell surface markers by measuring the modulation in transit time of the cells across the micropore (Carbonaro et al., 2008).

The majority of the above electrical detection techniques, primarily rely on detection of target cells based on the increase in impedance across a microchannel or measurement electrodes, which results from a decrease in the ionic current passing between electrodes, which occurs due to a partial occlusion of the ions passing between the electrodes due to the presence of the cell. Several other groups have demonstrated detection and recognition of target cells based on probing the impedance inside the cell by measuring impedance spectrum at frequencies greater than 1 MHz (Gawad et al., 2001). Among many works, for example, Frazier et al. demonstrated differentiation between tumor cells and non-tumorigenic cells (Han et al., 2007). Sohn et al. (2000) demonstrated capacitance cytometry where cells are sorted based on the charge inside the cell. In this work, we propose electrical detection of the presence of cells based on measuring the capacitance immediately inside (within 30 nm) the cell surface. The proposed probe is sensitive to the dielectric properties directly above the sensor surface.

In order to perform this measurement, we use a nanoscale electronic probe, which we refer to as the nanoneedles. We previously showed the utility of this sensor for label-free detection of proteins and nucleic acids (Esfandyarpour et al., 2013c, d). Here we demonstrate the applicability of this platform to measuring the presence of target cells bound to the sensor surface. The nanoneedle biosensor structure consists of two conductive layers with an insulator layer in between with a protective oxide layer above of the sensors (Fig. 1A and B). This top oxide layer is to prevent the exposure of conductive electrodes to the solution. There is also a thermally grown oxide underneath the bottom electrode to insulate the bottom electrode from the substrate.

Various thicknesses and geometrical designs of nanoneedle biosensors have been fabricated and tested. The thickness of top oxide layer, top electrode, middle oxide layer, bottom electrode and the bottom oxide layer are 20, 100, 30, 100, and 250 nm, respectively, and the sensor width is 3 μm (Esfandyarpour et al., 2012, 2013a). The active sensing

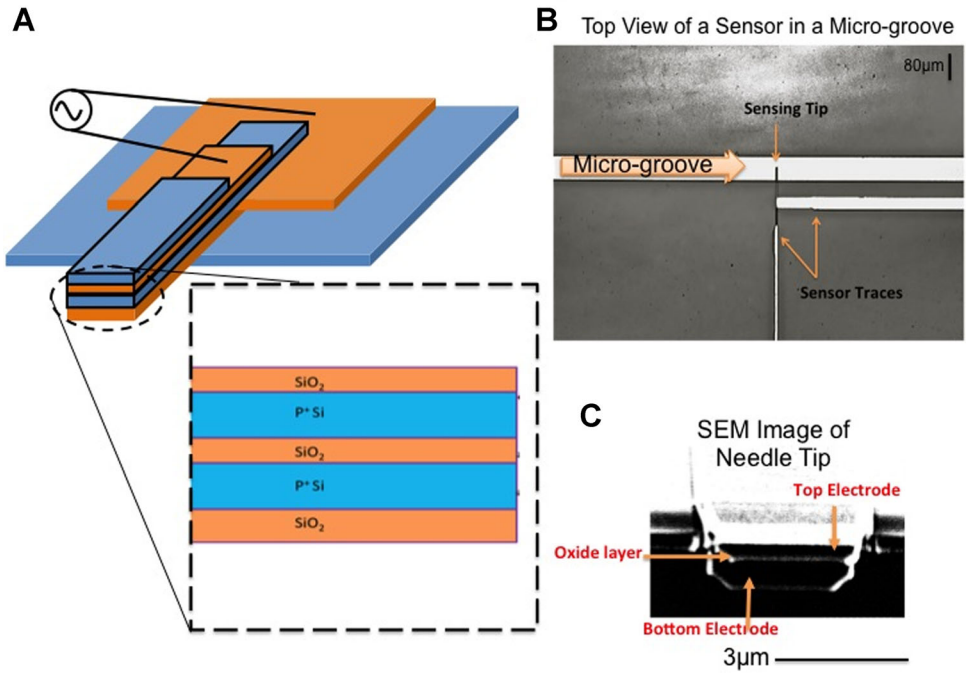

Figure 1. **A**: Three-dimensional schematic of nanoneedle biosensor with side view of sensor tip zoomed in. **B**: Optical micrograph of top view of sensor suspended in microfluidic groove. The sensor resides in a well of roughly 4 mm in diameter. The sample is pipetted into the well. **C**: SEM image of needle tip from front side.

region of the device is the middle oxide layer. Thus the thickness of that is the critical factor that determines the sensitivity of the sensor. First, the antibody against the target cell of interest can be immobilized on the tip of the sensor and then when the binding of target cells to the probe molecules occurs, the measured impedance between the electrodes gets modulated. In general, the presence of the cells non-specifically modulates the impedance, thus it is necessary to perform a wash step after binding to remove the unbound cells from the sensor surface. By comparing the impedance after the wash step with the impedance before cell loading, one can quantify binding of the cells.

We envision the sensor presented in this manuscript ultimately would be downstream a microfluidic sample preparation platform which would deliver a more purified and pre-concentrated sample to our proposed biosensor. Our aim in this manuscript is to discuss the biosensor itself and physical mechanisms behind the successful sensing of target cells, rather than the cellular detection platform as a whole. In this manuscript, we discuss the device physics and equivalent circuit model of the sensor, then we demonstrate a proof of concept of our sensor's ability to specifically detect target cells.

Device Fabrication

Horizontal nanoneedle biosensors were fabricated on a 4-in. wafers as explained below (Fig. 1C). The fabrication procedure was discussed previously in detail (Esfandyarpour et al., 2013a,b). Here we will discuss it again briefly. We started with an un-doped silicon wafer, followed by thermal growth of 250 nm of silicon dioxide on the silicon substrate. The resist for masking the bottom electrode was then patterned using photolithography. This step was followed by deposition of 100 nm of polysilicon using low-pressure chemical vapor deposition (LPCVD) to be used as the electrode. We used PH3 with a flow rate of 10 sccm, deposition time was 90 min and then it was annealed at 1,000°C for 30 min to lower the sheet resistance. Next, 30-nm thick SiO_2 layer was thermally grown on the bottom p+-silicon layer. Another 100-nm p+-silicon layer was deposited by using LPCVD as the top electrode. This step was followed by another phosphorus doping step to achieve the same conductivity as the bottom electrode. A top protective silicon dioxide layer (20-nm thick) was then deposited using plasma enhanced chemical vapor deposition (PECVD). In the next step, nanoneedle tips were expose by dry etching of the 30-nm top-SiO_2 layer, the 100-nm top p+-silicon layer, the30-nm middle oxide layer, and the 100-nm bottom p+-silicon layer down to bottom SiO_2 layer. This step was done to form a sharp edge on the nanoneedle sensor tip and to ensure that sensor tip electrodes in the channel are not covered with the oxide. Another etch step was performed to etch out the channel below the bundle of nanoneedles. Afterwards, the last etch step was performed to expose the bonding pads to enable access for measurements and wire bonding.

Circuit Model

We have developed a full circuit model to characterize and understand the interface of the nanoneedle sensor with the electrolyte as shown in Figure 2A. We can use this model to understand the response of the sensor in the presence of cells. Our electrode/electrolyte interface has various parasitic impedance components. In the model presented in this manuscript, we focus primarily on the impedance components at the interface of the electrode and electrolyte and not the impedance of the body of this sensor as these components do not change with the binding of a cell to the sensor surface. Above the electrodes and the insulator we have a double layer resulting from accumulation of ions in the electrolyte at each surface (metal and oxide). The electrical double layer consists of two layers, the stern layer, which is an adsorbed fixed layer, and also a diffuse layer. The stern layer consists of the ions that are adsorbed to the surface and are estimated to be concentrated roughly 1 nm from the sensor surface. The diffuse layer results because of the condition of charge neutrality. That is, another layer of ions accumulates in order to neutralize the charge in the stern layer. The thickness of the stern layer is generally concentration independent, whereas that of the diffuse layer is related inversely to the electrolyte concentration. When the salt concentration is low (<0.01 mM), the diffuse layer increases in size to be on the order of 10 nm (Hong et al., 2004), thus the capacitance becomes smaller than the stern layer capacitance and thus dominates the double layer capacitance. Based on the fact that

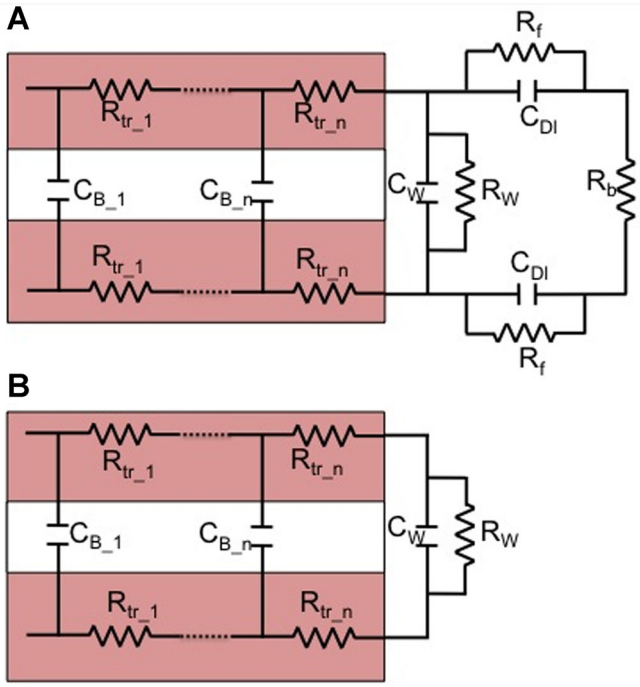

Figure 2. **A**: Complete circuit model of sensor and electrolyte interface. **B**: Simplified sensor circuit model.

we are using DI water as our electrolyte, the double layer is estimated to be on the order of 10 nm. This has several implications for our model. The first parasitic impedance is an interface resistance and a capacitance in between the electrodes, which we refer to as the wall capacitance and resistance (C_w and R_w). This is resulting from the fringing field between our electrodes, which extends into our electrolyte on a similar length scale as our double layer. The out of phase response affects C_w and the in-phase response affects R_w. The tunneling of electrons from the conductive electrodes into the biomolecules present at the active sensing region also affects the wall resistance (R_w). In parallel to these two components, we have another loop, which consists of the double layer capacitance (C_{dl}) at the surface of each metal electrode. In parallel to the double layer capacitance is the faradaic resistance (impedance) or the electron transfer resistance (R_f). This results from tunneling of electrons from the electrodes into the bulk electrolyte. In series with this is the bulk solution resistance (R_b), which results from the resistivity of the electrolyte.

Here the electrical response of the cells measured using our sensor is due to change in the relative permittivity at the sensor interface, which affects the imaginary component of the measured impedance. The presence of the biomolecules results in an increase in relative dielectric permittivity ($\kappa\varepsilon_{sol}$) of the solution at the sensor interface, thus resulting in an increase in capacitance and thus a decrease in impedance measured. This main effect is elaborated in more detail below.

The dominant phenomenon, which affects the out of phase (imaginary) AC response of the impedance, is the change in the wall capacitance at the sensor interface (C_w), which is affected by the change in relative dielectric permittivity of the solution. The cell consists of nucleic acids, proteins, and other charged molecules, which affect the relative dielectric permittivity at the sensor interface. For example, in the case of nucleic acids, the relative dielectric permittivity of the solution is explicitly affected by DNA dipole moment (DNA length and charge) and concentration of the DNA. The changes in the extracted wall capacitance C_w, which represents the DNA capacitance due to the movement of the counterion charges around the DNA backbone (dielectric relaxation of DNA dipoles), varied with changes in concentration of our DNA solutions. Changes in wall capacitance result in change in the imaginary component of the measured impedance (Liu et al., 2008). Similar mechanisms are at play for proteins resulting in a decrease in impedance as protein concentration increases at the electrode surface. Proteins on the surface of the cell membrane or the cell wall will affect the impedance at the sensor surface significantly.

In order to determine the contribution of the above-mentioned mechanisms contributes to the impedance changes, we measured the impedance spectrum across the nanoneedle sensor as shown in Figure 3 and extracted the parasitic impedance components. In Figure 3, we have shown the spectrum for the bare sensor in water. The optimum region for sensor operation occurs between 1–100 kHz given that the largest difference in response between water and cell solution occurs. As mentioned, in a low salt concentration electrolyte the double layer is 10-nm thick, thus the impedance resulting from the double layer capacitance (C_{dl}) can be calculated to be ~1 GΩ at 15 kHz. By measuring the impedance at 1 Hz and calculating C_{dl} at this frequency, the faradaic impedance (due to tunneling of electrons from the electrodes to the electrolyte is determined. The total impedance at 1 Hz is 0.5 GΩ, meaning that R_f in series with R_b (both frequency independent) can be no less than 0.5 GΩ across the whole spectrum. This means that the equivalent

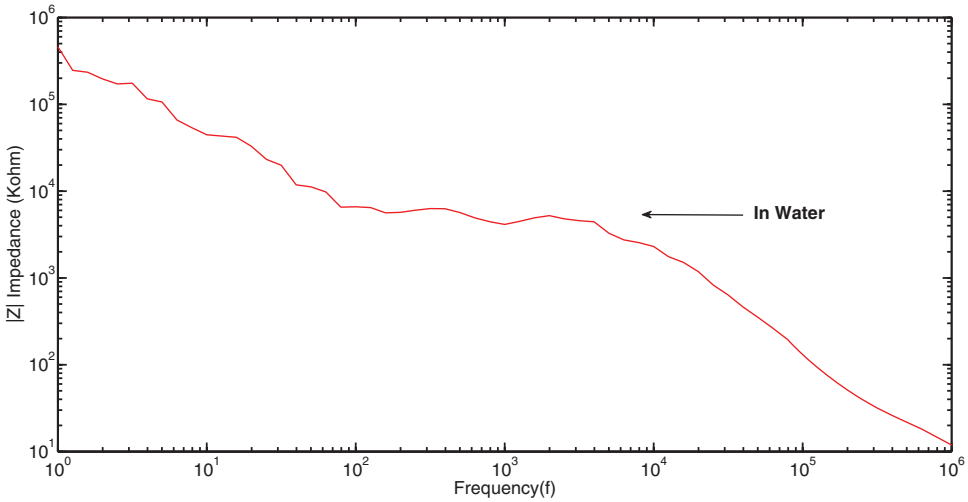

Figure 3. Impedance spectrum for bare sensor in water. Based on experimental optimization maximum modulation of impedance occurs at $f = 15$ KHz, thus device was operated at this frequency for all measurements.

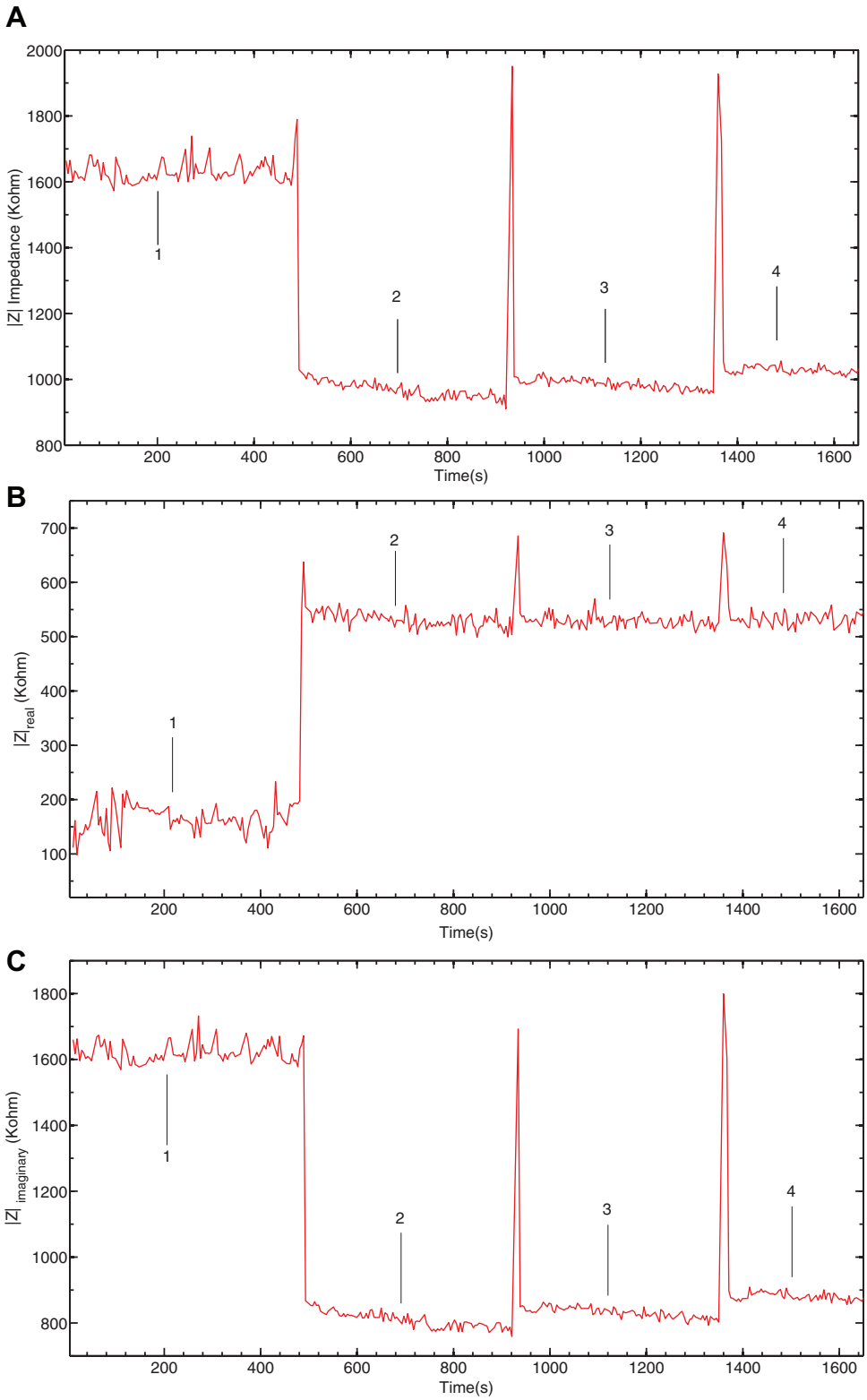

Figure 4. **A**: Magnitude of impedance verses time for yeast cells injected on non-functionalized sensor surface. (1) DI water, (2) 100×10^4 cells/mL, (3) 20×10^4/mL, (4) 2×10^4/mL. **B**: Real component of impedance verses time for yeast cells injected on non-functionalized sensor surface. **C**: Imaginary component of impedance verses time.

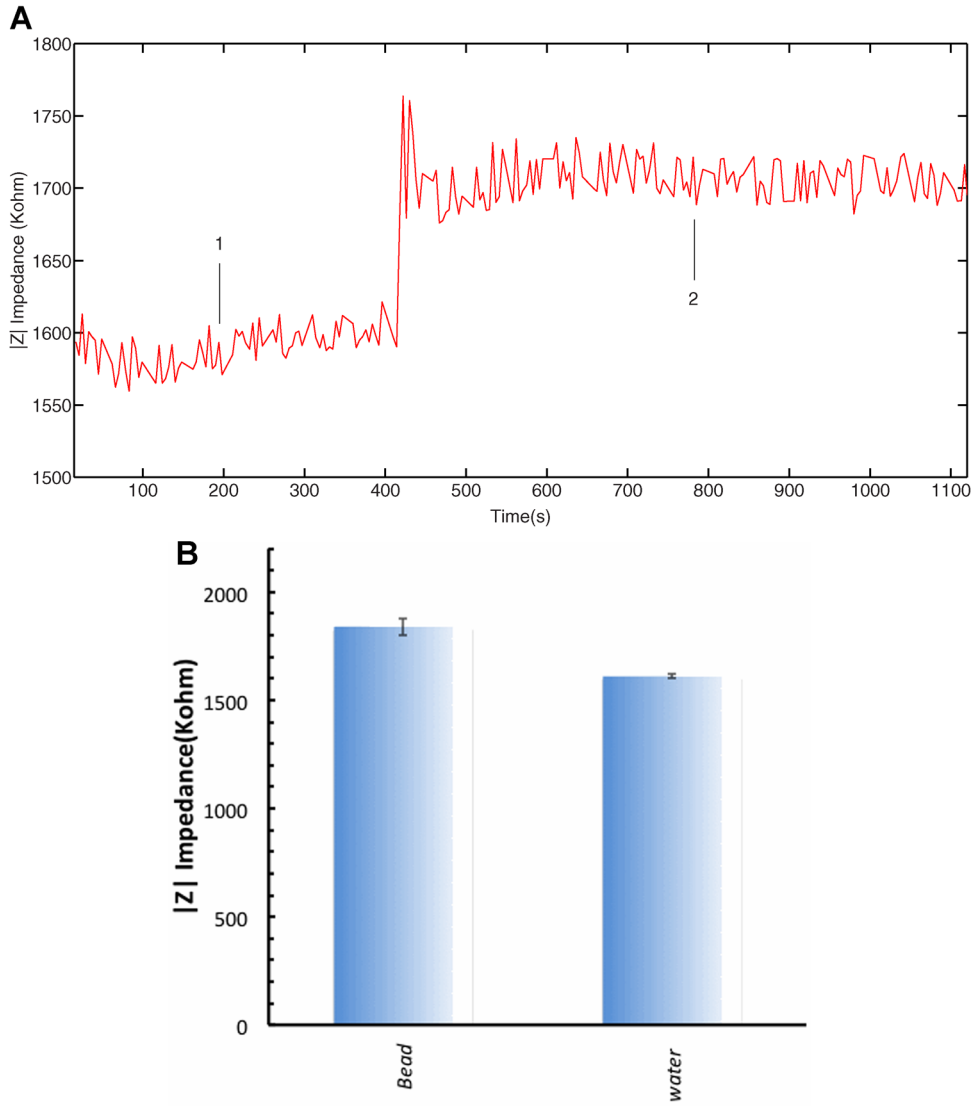

Figure 5. **A**: Control experiment of impedance verses time for polystyrene bead injected on to sensor (1) DI water, (2) polystyrene beads. **B**: Average impedance magnitude value with error bars for polystyrene bead control experiment.

impedance of C_{dl} and R_f in parallel with each other and in series with R_b has to also be greater than 0.5 GΩ. Comparing this to the total impedance of the sensor at 15 kHz which is 3.6 MΩ, we are able to assume that the loop containing C_{dl}, R_f and R_b is essentially an open circuit allowing us to simplify our model significantly as shown in Figure 2B. This simplifies the model to C_w and R_w in parallel, thus allowing us to understand which source to attribute the changes in impedance. The change in the real component of the impedance results primarily from the modulation of the wall resistance (R_w), which is affected by the blockage of ions passing between the electrodes. The change in the imaginary component on the other hand is fully dominated by modulation of the wall capacitance (C_w), which is affected by the increase in relative dielectric permittivity ($\kappa\varepsilon_{sol}$) of the solution at the sensor interface due to the presence of the biomolecules at the surface of the cell and inside the cell. As mentioned the relative dielectric permittivity ($\kappa\varepsilon_{sol}$) is affected by both the dipole moment and concentration of the biomolecules.

Cell Culturing and Preparation

Sacharomyces ceresiae was used in our experiments as a proof of concept. The strain was slanted on an YPD (Yeast extract Peptone Dextrose) petri dish (1% yeast extract, 2% bactopeptone, 2% glucose). The YPD dishes were placed in a 37°C incubator overnight. One colony was taken out of the petri dish and transferred into 5 mL of YPD in a test tube. The test tube was placed in a 37°C incubator overnight. The number of cells was 10^6 cells/μL.

Experimental Results and Discussion

As a proof of concept, we studied the behavior of this sensor in the presence of cells by using yeast cells (Fig. 4A). Yeast cell solutions ranging from 100 to 10^5 cells/μL were injected onto the sensor surface, resulting in a decrease in impedance with increasing cell concentration similar to the results previously obtained with protein and DNA (Esfandyarpour et al., 2013d). A Versa STAT3 potentiostat was used to measure the impedance while the biomolecules were present close to the sensor tip. A sinusoidal voltage signal (100 mV RMS, 15 KHz) was applied to the top electrode and the current entering the bottom electrode was measured to calculate the impedance. Initially, 100 cells/μL were injected resulting in a drop in impedance. Afterwards the sensor was washed off and dried, and then 10^5 cells/μL were injected resulting in a decrease in impedance. The impedance across the device decreased with increasing concentration of cells. This experiment was performed three times demonstrating similar results. Normally, it would be expected that cells in an aqueous buffer would show a similar behavior; however, the injection of cells onto the sensor surface showed the opposite trend, which demonstrates that the electrical response across the electrodes is being affected by the relative dielectric permittivity and charged polyelectrolytes inside the cell. The charged molecules both on the surface and inside the cell are resulting in an increase in the relative dielectric permittivity inside the cell. The other potential effect is blockage of ionic current passing between the electrodes. We are able to decouple these two effects from each other by analyzing the real (Fig. 4B) and imaginary components (Fig. 4C) of the impedance. The presence of the cells on the sensor surface results in a decrease in the imaginary component of the impedance which corresponds to an increase in the wall capacitance, whereas the real component of the impedance experiences no change. This means that the dominant mechanism affecting the sensor response is the change in wall capacitance at the sensor surface.

As a control experiment to verify the physical mechanism resulting in the electrical response of the sensor we injected polystyrene beads (which have fully insulative electrical properties) instead of cells. As shown in Figure 5A, an increase in impedance was observed as opposed to the decrease in impedance seen with injection of cells. The average impedance over three repetitions along with the error bar is shown in Figure 5B. The presence of the beads on the sensor surface results primarily in a change in the imaginary component of the impedance corresponding to a decrease in the capacitance. Similar to yeast cells, the change in the real component is insignificant.

In order to demonstrate the utility of this technique for the affinity based bio-sensing by emphasizing target cell capturing and cell detection, we used yeast cells as our target cells, and Concanavalin A (ConA), a glycoprotein with affinity for the sugar molecules on yeast, in place of antibodies. Figure 6 shows our experimental result for the real time detection of yeast cell capture using ConA as the receptor. A low pass filter has been applied to reduce the noise of the measurement. The steps are explained below.

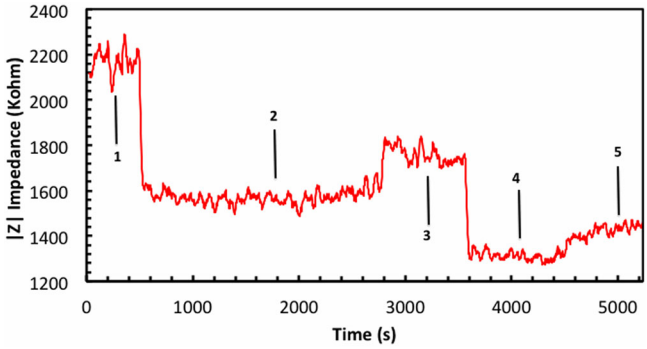

Figure 6. Target cell capture and detection experiment demonstrating specific detection of yeast cells. (1) DI water. (2) Immobilization of ConA on surface. (3) Wash with DI water. (4) Injection of yeast cells. (5) Wash with DI water. Final impedance value (5) is less than washed ConA functionalized surface (3) demonstrating cell capture and detection.

First, ConA was diluted to the concentration of 100 mg/mL and was then injected into the well which was located on top of the sensor. ConA was immobilized on the active region of the sensor using physical adsorption for 30 min. The impedance of the sensor was measured during the process as shown in Figure 6 step 1. Afterwards we aspirated the measurement well and washed the sensor with water. As seen in Figure 6 in step 2, the impedance of the sensor increased. The next step was injection of yeast cells with a concentration of 10^8 cells/mL. In order to allow the yeast cells to get captured by the receptors on the sensor active region, we incubated the cell suspension for 15 min. We again aspirated the fluid in the measurement well and performed another wash step, which again increased the measured impedance. The final impedance levels after both wash steps (after ConA adsorption and after yeast cells binding) are compared with each other to quantify the number of cells captured by the ConA molecules at the sensor surface.

Optical verification of yeast cells specifically captured on the sensor surface before (Fig. 7A) cell injection and after cell injection and the final wash step is shown in Figure 7B which not only confirms the physical immobilization of ConA molecules to the sensor surface but also confirms the capturing of yeast cells. An electrical control experiment was also performed where yeast cells are injected onto a non-functionalized sensor surface and then washed while the impedance is measured in real time.

Figure 8 shows the average value of the impedance with the error bars for three states: the non-functionalized sensor in water, cells injected onto the sensor, and finally the sensor response after the unbound cells have been washed off. The presence of the cells results in a drop in impedance however, the impedance value returns back to the original baseline after the cells have been washed off, verifying that the change in signal seen in Figure 6 results from cells specifically bound

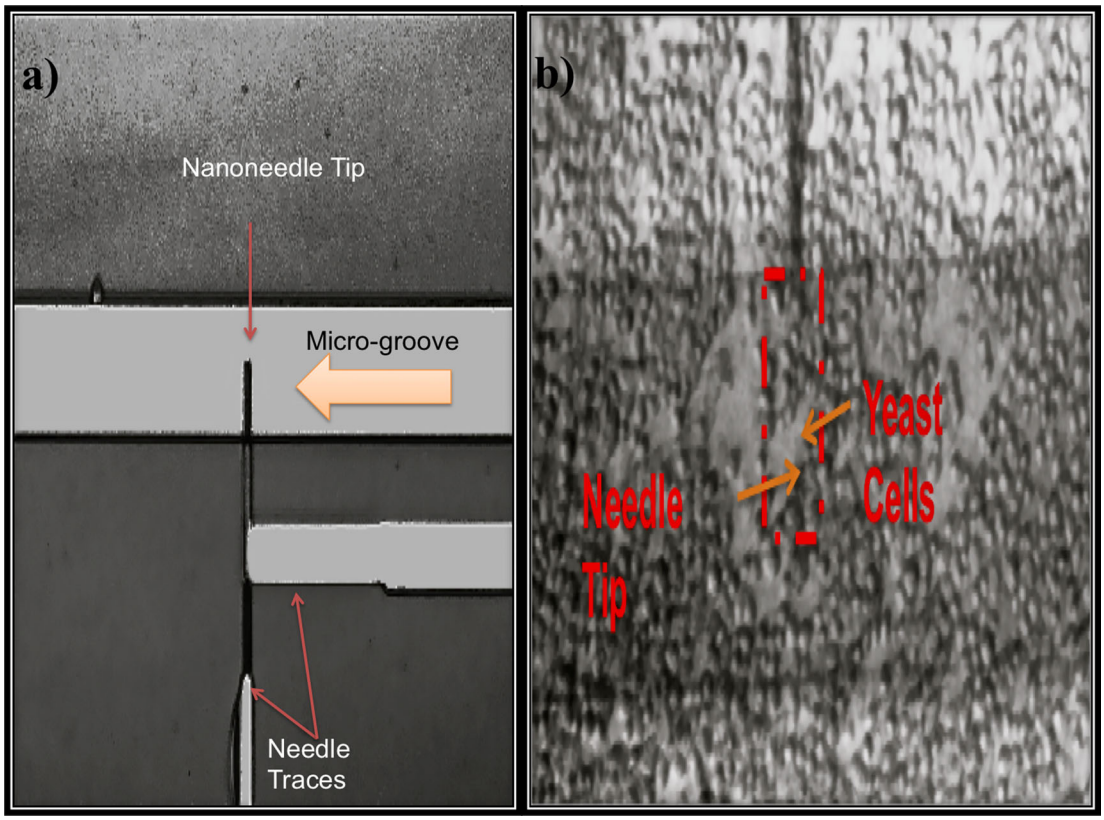

Figure 7. **A**: Optical micrograph of bare nanoneedle sensor. **B**: Image of yeast cells captured on functionalized surface.

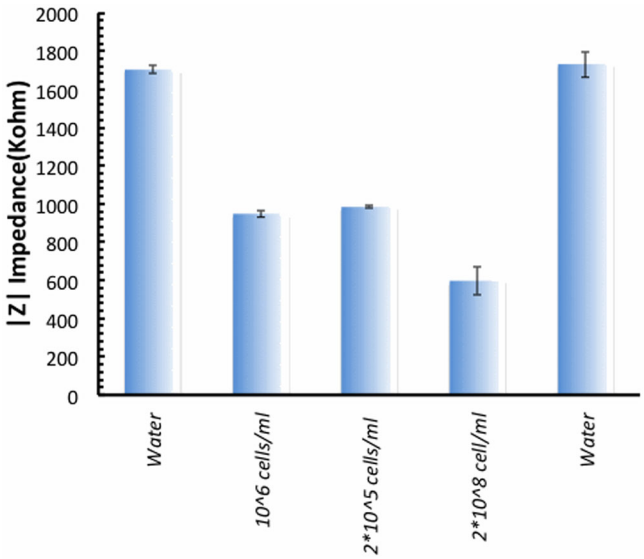

Figure 8. Control experiment to demonstrate specificity of yeast cell detection. Average impedance values (three experiments) with error bars for series of injections starting with DI water then 10^6 cells/mL then 2×10^5 cells/mL, then 2×10^8 cells/mL, and then DI water again. Increased concentration of cells results in drop in impedance. Since the cells were not specifically bound, the final wash step with water results in all cells being removed from the sensing area resulting in the impedance rising back up to its original value.

to the sensor surface due to interactions between ConA and the yeast cell surface.

Conclusion

We have presented a nanoelectronic probe capable of measuring the dielectric properties of cells and have demonstrated the proof of concept for affinity-based sensing of yeast cells. Contrary to traditional impedance sensing of cells, where the presence of cells on the active sensing region results in an increase in impedance due to blockage of ions passing between the electrodes, the presence of cells in the active sensing region of the nanoneedle results in a decrease in impedance. This decrease in impedance results from an increase in the relative dielectric permittivity at the surface of the sensor. While we demonstrated proof of concept using yeast cells, we emphasize that this sensing concept can be applied to affinity based sensing of a wide range of different types of cells. In addition to this, since the proposed sensor has a rigid nanostructure, one can envision inserting the thin functionalized needle inside of a single living cell to directly monitor gene and protein expression. Fabrication of the nanoneedle arrays allows us to monitor an event instantaneously in a large area and also perform multiplexed detection. The signal to noise ratio of the sensor can be improved by on chip integration of the sensors with CMOS amplification electronics resulting in a single portable device suitable for point-of-care diagnostics.

References

Aaron SD, Kottachchi D, Ferris WJ, Vandemheen KL, Denis MLS, Plouffe A, Doucette SP, Saginur R, Chan FT, Ramotar K. 2004. Sputum versus bronchoscopy for diagnosis of *Pseudomonas aeruginosa* biofilms in cystic fibrosis. Eur Respir J 24(4):631–637.

Carbonaro A, Mohanty SK, Huang H, Godley LA, Sohn LL. 2008. Cell characterization using a protein-functionalized pore. Lab Chip 8(9):1478–1485.

Chaurey V, Rohani A, Su YH, Liao KT, Chou CF, Swami NS. 2013. Scaling down constriction-based (electrodeless) dielectrophoresis devices for trapping nanoscale bioparticles in physiological media of high-conductivity. Electrophoresis 34(7):1097–1104.

Chen GD, Fachin F, Fernandez-Suarez M, Wardle BL, Toner M. 2011. Nanoporous elements in microfluidics for multiscale manipulation of bioparticles. Small 7(8):1061–1067.

Emaminejad S, Javanmard M, Dutton RW, Davis RW. 2012. Microfluidic diagnostic tool for the developing world: Contactless impedance flow cytometry. Lab Chip 12(21):4499–4507.

Esfandyarpour R, Esfandyarpour H, Javanmard M, Harris JS, Davis RW. 2012. Electrical detection of protein biomarkers using nanoneedle biosensors. MRS Proceedings, Vol. 1414. Cambridge University Press.

Esfandyarpour R, Esfandyarpour H, Harris JS, Davis RW. 2013a. Simulation and fabrication of a new novel 3D injectable biosensor for high throughput genomics and proteomics in a lab-on-a-chip device. Nanotechnology 24(46):465301.

Esfandyarpour R, Esfandyarpour H, Javanmard M, Harris JS, Davis RW. 2013b. Microneedle biosensor: A method for direct label-free real time protein detection. Sensor Actuat B Chem 177:848–855.

Esfandyarpour R, Javanmard M, Harris JS, Davis RW. 2013c. Thin film nanoelectronic probe for protein detection. MRS Proceedings, Vol. 1572. Cambridge University Press.

Esfandyarpour R, Javanmard M, Koochak Z, Esfandyarpour H, Harris JS, Davis RW. 2013d. Label-free electronic probing of nucleic acids and proteins at the nanoscale using the nanoneedle biosensor. Biomicrofluidics 7(4):044114.

Gawad S, Schild L, Renaud P. 2001. Micromachined impedance spectroscopy flow cytometer for cell analysis and particle sizing. Lab Chip 1(1):76–82.

Han A, Yang L, Frazier AB. 2007. Quantification of the heterogeneity in breast cancer cell lines using whole-cell impedance spectroscopy. Clin Cancer Res 13(1):139–143.

Hong J, Yoon DS, Park M-I, Choi J, Kim TS, Im G, Kim S, Pak YE, No K. 2004. A dielectric biosensor using the capacitance change with AC frequency. Jpn J Appl Phys 43:5639–5645.

Javanmard M, Talasaz AH, Nemat-Gorgani M, Pease F, Ronaghi M, Davis RW. 2007. Targeted cell detection based on microchannel gating. Biomicrofluidics 1:044103.

Javanmard M, Babrzadeh F, Nyrén P, Davis RW. 2012. Improvement in cell capture throughput using parallel bioactivated microfluidic channels. Biomed Microdevices 14(4):625–629.

Khaw BA, Scott J, Fallon JT, Cahill SL, Haber E, Homcy C. 1982. Myocardial injury: quantitation by cell sorting initiated with antimyosin fluorescent spheres. Science 217(4564):1050–1053.

Liu Y-S, Banada PP, Bhattacharya S, Bhunia AK, Bashir R. 2008. Electrical characterization of DNA molecules in solution using impedance measurements. Appl Phys Lett 92(14):143902–143902-3.

Mittal S, Wong IY, Deen WM, Toner M. 2012. Antibody-functionalized fluid-permeable surfaces for rolling cell capture at high flow rates. Biophys J 102(4):721–730.

Moon S, Keles HO, Ozcan A, Khademhosseini A, HÃggstrom E, Kuritzkes D, Demirci U. 2009. Integrating microfluidics and lensless imaging for point-of-care testing. Biosens Bioelectron 24(11):3208–3214.

Mostafalu P, Sonkusale S. 2013. Flexible and transparent gastric battery: Energy harvesting from gastric acid for endoscopy application. Biosens Bioelectron 54:292–296.

Nagrath S, Sequist LV, Maheswaran S, Bell DW, Irimia D, Ulkus L, Smith MR, Kwak EL, Digumarthy S, Muzikansky A. 2007. Isolation of rare circulating tumour cells in cancer patients by microchip technology. Nature 450(7173):1235–1239.

Sohn LL, Saleh OA, Facer GR, Beavis AJ, Allan RS, Notterman DA. 2000. Capacitance cytometry: Measuring biological cells one by one. Proc Natl Acad Sci 97(20):10687–10690.

Stott SL, Hsu C-H, Tsukrov DI, Yu M, Miyamoto DT, Waltman BA, Rothenberg SM, Shah AM, Smas ME, Korir GK. 2010. Isolation of circulating tumor cells using a microvortex-generating herringbone-chip. Proc Natl Acad Sci 107(43):18392–18397.

Talasaz AH, Powell AA, Huber DE, Berbee JG, Roh K-H, Yu W, Xiao W, Davis MM, Pease RF, Mindrinos MN. 2009. Isolating highly enriched populations of circulating epithelial cells and other rare cells from blood using a magnetic sweeper device. Proc Natl Acad Sci 106(10):3970–3975.

Zhu HY, Mavandadi S, Coskun AF, Yaglidere O, Ozcan A. 2011. Optofluidic fluorescent imaging cytometry on a cell phone. Anal Chem 83(17):6641–6647.